

Ferromagnetism and giant magnetoresistance in zinc-blende FeAs monolayers embedded in semiconductor structures

Le Duc Anh^{1,2,3*}, Taiki Hayakawa¹, Yuji Nakagawa⁴, Hikari Shinya^{5,6,7}, Tetsuya Fukushima^{7,8,9}, Masaki Kobayashi^{1,9}, Hiroshi Katayama-Yoshida⁹, Yoshihiro Iwasa^{4,10}, and Masaaki Tanaka^{1,9,*}

¹*Dept. of Electrical Engineering and Information Systems, The University of Tokyo, Japan*

²*Institute of Engineering Innovation, The University of Tokyo, Japan*

³*PRESTO, Japan Science and Technology Agency, Japan*

⁴*QPEC & Dept. of Applied Physics, The University of Tokyo, Japan*

⁵*Research Institute of Electrical Communication, Tohoku University, Japan*

⁶*Center for Spintronics Research Network (CSRN), Tohoku University, Japan*

⁷*Center for Spintronics Research Network (CSRN), Osaka University, Japan*

⁸*Institute for Solid State Physics, The University of Tokyo, Japan*

⁹*Center for Spintronics Research Network (CSRN), The University of Tokyo, Japan*

¹⁰*RIKEN Center for Emergent Matter Science (CEMS), Japan*

**E-mail: anh@cryst.t.u-tokyo.ac.jp*

masaaki@ee.t.u-tokyo.ac.jp

Material structures containing tetrahedral FeAs bonds, depending on their density and geometrical distribution, can host several competing quantum ground states ranging from superconductivity to ferromagnetism. Here we examine structures of quasi two-dimensional (2D) layers of tetrahedral Fe-As bonds embedded with a regular interval in a semiconductor InAs matrix, which resembles the crystal structure of Fe-based superconductors. Contrary to the case of Fe-based pnictides, these FeAs/InAs superlattices (SLs) exhibit ferromagnetism, whose Curie temperature (T_C) increases rapidly with decreasing the InAs interval thickness t_{InAs} ($T_C \sim t_{\text{InAs}}^{-3}$), and an extremely large magnetoresistance up to 500% that is *tunable* by a gate voltage. Our first principles calculations reveal the important role of disordered positions of Fe atoms in the establishment of ferromagnetism in these

quasi-2D FeAs-based SLs. These unique features mark the FeAs/InAs SLs as promising structures for spintronic applications.

Tetrahedral FeAs-based materials have attracted much attention in recent years since the discovery of Fe-based high-temperature superconductors (Fe-based pnictides)^{1,2} and later, Fe-based high- T_C ferromagnetic semiconductors (FMSs)³⁻¹¹. In Fe-based superconductors where Fe-As bonds are confined in 2D monolayers (MLs), the magnetic ground state of the Fe spins is antiferromagnetic by super-exchange interaction, and superconductivity appears upon doping carriers or applying pressure. On the other hand, in Fe-based FMSs such as (In,Fe)As where Fe-As bonds are distributed randomly in a three-dimensional (3D) InAs semiconductor matrix, the Fe spins couple ferromagnetically via interactions with electron carriers^{3,6,7}. These results strongly suggest that the density and geometrical distribution of the Fe-As bonds are crucial in determining the transport and magnetic properties of their nanostructures. To understand the underlying physics behind these fascinating structures, it is necessary to systematically study their transport and magnetic properties when varying the distribution of Fe-As bonds. In particular, it is required and important to investigate the nature of the magnetic ground state in the 3D-2D crossover limit when the Fe-As bonds are confined in 2D ultrathin layers embedded in the InAs matrix at a regular distance, which resembles the case of both the Fe-based pnictides and (In,Fe)As FMS (Fig. 1a).

A pioneering theoretical work by Griffin and Spaldin¹² suggested that in superlattice (SL) structures of FeAs tetrahedral layers embedded in a zinc-blende semiconductor matrix, the antiferromagnetic phase should be the magnetic ground state as in the Fe-based superconductors. The work also revealed a half-metallic band structure in the hypothetical ferromagnetic phase of zinc blende FeAs. On the other hand, in (In₁₋

x ,Fe $_x$)As, where Fe atoms ($x = 1 - 10$ %) are randomly distributed and partially replace the In sites and thus the local Fe density is much less than that of the FeAs monolayer-based SLs, previous experimental works revealed electron-induced ferromagnetism with Curie temperature (T_C) as high as 120 K^{13,14}. This result was striking since the s - d exchange interaction was hitherto believed to be extremely weak^{15,16}. In fact, (In,Fe)As is the first n-type electron-induced III-V FMS, which provides an important missing piece for spin device applications based on semiconductors. Various unique and essential features have been realized in this material, such as quantum size effects^{5,6}, large s - d exchange interaction energy^{4,6}, large spontaneous spin splitting in the conduction band⁷, and proximity-induced superconductivity over a very long distance (~ 1 μm)^{13,14}. A notable feature in (In,Fe)As and other Fe-based FMSs is the rapid increase of T_C over the room temperature with increasing the Fe density¹¹. Indeed, first principles calculations suggested that the ferromagnetic interactions between the Fe atoms in InAs can be strongly enhanced if the distance between the Fe atoms can be reduced to that between the next-nearest neighbor sites, via super-exchange interactions¹⁷. Furthermore, enhancement of ferromagnetism has also been reported in similar magnetic “digital alloys” of Mn-doped FMSs^{18,19,20}. These recent experimental and theoretical findings thus suggested that in the FeAs-based SLs, a ferromagnetic ground state is favorable. These contradicting theoretical predictions on the dependence of the magnetic properties of Fe doped InAs on the geometrical distribution of the Fe-As bonds thus strongly call for experimental verifications.

In this work, we study the epitaxial growth and properties of SL structures of FeAs quasi-2D ultrathin layers embedded in an InAs semiconductor matrix at a regular distance (t_{InAs}). Contrary to the first principle calculation of ref.12 and the case of Fe-based

pnictides, we find that these FeAs/InAs SLs exhibit strong ferromagnetism whose T_C increases rapidly with decreasing the InAs interlayer thickness t_{InAs} ($T_C \propto t_{\text{InAs}}^{-3}$), with a very high magnetic moment per Fe atom ($4.7 - 4.9 \mu_B$, where μ_B is Bohr magneton). We also observe in these SL structures an extremely large magnetoresistance up to 500%, which is *tunable* by a gate voltage. Our microstructure characterizations and first principles calculations reveal that disordered positions of Fe atoms play a key role in establishing the ferromagnetic ground state. These unique features indicate that these FeAs/InAs SLs are promising for spintronic applications.

RESULTS

Growth and crystal structure of FeAs/InAs SL structures

Growth of FeAs/InAs SLs with zinc-blende crystal structure is highly challenging due to the low solubility of Fe in III-V semiconductors, which easily causes atomic segregation and phase separation. Indeed, there is no report on the zinc-blende FeAs bulk structure to date although it is theoretically predicted to host a half-metallic band structure¹². In this work, we grew FeAs/InAs SL structures on InAs (001) or semi-insulating GaAs (001) substrates by employing a special technique of low-temperature molecular-beam epitaxy (LT-MBE). In the growth on GaAs substrates, as illustrated in Fig. 1a, we grow a 500 nm-thick AlSb layer at a growth temperature $T_S = 470^\circ\text{C}$ on a 10 nm-thick AlAs / GaAs (001) substrate prior to the growth of the SL structures to obtain a smooth and lattice-matched buffered layer. Then T_S is decreased to 220°C and we grow the FeAs/InAs SL structure, consisting of N periods of InAs (t_{InAs} MLs) / FeAs (nominally 1 ML), and finally an InAs cap layer (t_{InAs} MLs). The InAs and FeAs layers are grown at growth rates of 500 nm/h and 250 nm/h, respectively, for which we calibrated the Fe flux

to be exactly a half of the In flux (see Methods). We grew a series of samples, numbered from A1 to A4, with the thickness parameters $(N, t_{\text{InAs}}) = (1, 20), (3, 10), (5, 7), (7, 5)$, respectively. Here, the total thicknesses of the FeAs/InAs SLs in all the samples (A1 - A4) are nearly fixed at 41 - 47 MLs, which are equal to 12.4 - 14 nm. Therefore the distance between the FeAs layers, t_{InAs} , is inversely proportional to N . For reference, we also grew sample A0 consisting of a 12-nm-thick structure of (In,Fe)As (6% Fe, 7 nm) / InAs (5 nm) on top of the AlSb buffer layer. The structure and T_C of all the samples are summarized in Table 1. In Fig. 1b we show the *in situ* reflection high energy electron diffraction (RHEED) patterns of the SL structure in sample A4 ($N = 7$). The RHEED patterns are very bright and streaky during the growth of the InAs layers, darken but remain the zinc-blende pattern during the growth of the FeAs layers, then well recovered during the growth of the next InAs layer. This indicates that the SL structures in all the samples are grown in a good 2D growth mode maintaining the zinc-blende crystal structure, and there is no sign of second-phase precipitation.

We examine the crystal structure and Fe distribution using scanning transmission electron microscopy (STEM) and energy-dispersive X-ray spectroscopy (EDX) mapping. Figure 1c shows the results of a sample consisting of a FeAs (nominally 1 ML) sandwiched between InAs layers, grown on an InAs (001) substrate using the same growth procedure and conditions explained above. Only the zinc-blende crystal structure of the host InAs is observed from the STEM lattice image (left panel of Fig. 1c). The STEM contrast is directly related to the atomic number, so that one can see a darker horizontal line with a line width of roughly 3 MLs corresponding to the FeAs layer. EDX mapping results of the Fe atoms also confirm the Fe distribution in a quasi-monolayer located at 10 nm from the surface (right panel of Fig. 1c). Along the growth direction z ,

the Fe concentration follows a normal distribution with a standard deviation $\sigma = 0.45$ nm, corresponding to 1.5 ML using the lattice constant of InAs (Fig. 3d). We note that the spatial resolution of EDX is 3 – 4 MLs, which is larger than σ . Therefore, we can conclude that ultrathin tetrahedral FeAs layers are successfully grown in a zinc-blende InAs matrix, and the Fe atoms are mainly confined within a thickness of 2 – 3 MLs.

Magnetic properties of the FeAs/InAs SL structures

We examine the magnetic properties of sample A0 – A4 using magnetic circular dichroism (MCD) and superconducting quantum interference device (SQUID) magnetometry. Figure 2a shows the MCD spectra of these samples measured at 5 K and under a magnetic field H of 1 T applied perpendicular to the film plane. The MCD spectra of the samples A1 – A4 exhibit very similar shapes with strongly enhanced peaks close to the optical transition energies at the critical points of the zinc-blende InAs band structure, E_1 (2.61 eV), $E_1 + \Delta_1$ (2.88 eV), E_0' (4.39 eV), and E_2 (4.74 eV)³. These features are similar to the MCD spectrum of the (In_{0.94}Fe_{0.06})As reference sample (A0) with the same thickness (12 nm). This result indicates that even when the Fe atoms are highly concentrated in the 2D ultrathin layers, the band structure of the SLs maintains the basic properties of the host InAs, such as the band gap and most of the band dispersions. This finding is consistent with their single-phase zinc-blende crystal structure revealed by STEM. Moreover, compared with the MCD spectrum of the (In_{0.94}Fe_{0.06})As reference sample, the MCD intensity of the FeAs/InAs SL in sample A2, which has almost the same average Fe concentration (which is 6.9% = 3 MLs / 43 MLs), is three-fold stronger. This clearly indicates an enhancement of the magnetization and the spin splitting energy in the band structure of the FeAs/InAs SLs, probably because the Fe atoms are closely

distributed in the FeAs planes. The MCD intensity in sample A2, A3, A4 stays almost constant, which may be due to a short penetration depth of visible light in these structures (See Supplementary Note 4).

We estimate T_C of sample A1 – A4 by the Arrott plots²¹ of the MCD – H curves at different temperatures (Fig. 2b), whose results are summarized in Fig. 2c. All the samples exhibit ferromagnetism, contradicting the prediction of ref.12. Interestingly, T_C increases rapidly as the distance t_{InAs} between the FeAs MLs decreases, which can be approximately expressed as $T_C \propto t_{\text{InAs}}^{-3}$. This relation indicates that the interlayer magnetic interaction between the FeAs layers, which is likely mediated by electron carriers, play an important role in inducing the ferromagnetism. The inverse third power dependence of T_C on t_{InAs} can be understood qualitatively as follows: If we regard the total magnetic moment in each FeAs ML as a *macroscopic spin* \mathcal{S} , and define J_{ij} as the exchange interaction energy between the magnetic moments \mathcal{S} of the i th and j th FeAs MLs separated by a distance of $|i-j|t_{\text{InAs}}$, J_{ij} is proportional to $\sim |i-j|^{-2}t_{\text{InAs}}^{-2}$ as is well-known in magnetic multilayer systems with RKKY-like interlayer interaction²². Using the Heisenberg model, we have the following relation:

$$T_C \propto \frac{1}{2} \sum_{i,j=1(i \neq j)}^N J_{ij} \mathcal{S}^2 = \frac{S^2}{2t_{\text{InAs}}^2} \sum_{i,j=1(i \neq j)}^N \frac{1}{(i-j)^2} = \frac{S^2}{2t_{\text{InAs}}^2} \sum_{i=1}^N \frac{N-i}{i^2} . \quad (1)$$

We deduce from (1) that

$$T_C = A \left(\frac{N}{t_{\text{InAs}}^2} \sum_{i=1}^N \frac{1}{i^2} - \frac{1}{t_{\text{InAs}}^2} \sum_{i=1}^N \frac{1}{i} \right) , \quad (2)$$

where A is a proportional constant. In eq. (2), the first term is roughly 4 times larger than the second term for $N = 1, 3, 5, 7$. Therefore, considering the relationship $N \propto t_{\text{InAs}}^{-1}$, if we express T_C as $t_{\text{InAs}}^{-\gamma}$ the exponent γ is a value close to 3. As can be seen in Fig. 2c, the T_C values calculated using eq. (2) with $A = 190$ (open diamonds) well reproduce the

experimental results (pink circles). An important implication of this $T_C \propto t_{\text{InAs}}^{-3}$ relationship is that we would obtain a room-temperature ferromagnetism in the SLs with $t_{\text{InAs}} < 3$ MLs, which might be achievable by optimizing the growth conditions.

Another important feature of the FeAs/InAs SL structures is that they possess a large magnetic moment per Fe atom of 4.7 - 4.9 μ_B . As shown in Fig. 2d, the saturated magnetization in sample A2 – A4, measured at 10 K under a magnetic field perpendicular to the film plane by SQUID magnetometry, increases linearly with the number N of the FeAs layers. These impressive results might be induced by the 2D distribution of the Fe atoms, which are all neighboring to InAs at both the top and bottom interfaces. This lowers the symmetry around the Fe atoms, which can strongly enhance their orbital moment component to as high as that of an isolated Fe atom ($2\mu_B/\text{Fe}$)²³. This high value of magnetic moment also excludes the possibility of Fe clusters, which usually have a magnetic moment of only 2.2 μ_B/Fe atom (see Supplementary Note 1 and Supplementary Fig. S2). This is a huge improvement from the case of randomly Fe-doped (In,Fe)As, in which the magnetic moment per Fe atom is only 1.8 μ_B corresponding to a missing of 64% of the Fe magnetic moment³. This finding agrees well with the prediction of the first principles calculation that the ferromagnetic interactions between the Fe atoms in InAs can be strongly enhanced if the distance between the Fe atoms is reduced¹⁷.

Magnetoresistances (MR) in the FeAs/InAs SL structures

The transport properties of the FeAs/InAs SL structures, examined in patterned Hall bars of size $50 \times 200 \mu\text{m}^2$, also depend significantly on t_{InAs} . As shown in Fig. 3(a), the temperature dependence of the resistivity changes from metallic behavior in samples A1 and A2 to insulating behavior in samples A3 and A4. Particularly at low temperatures,

the resistivity drastically increases by 5 orders of magnitude when decreasing t_{InAs} from 20 MLs (sample A1) to 5 MLs (sample A4). However, the resistivity decreases significantly when we applied an external magnetic field \mathbf{H} perpendicular to the film plane. The decrease of resistivity by applying \mathbf{H} is particularly strong in the samples with high resistivity. Figure 3b shows magnetoresistance (MR), where the MR ratio is defined as $\text{MR}(H) = [R(0) - R(H)]/R(H) \times 100\%$, in sample A4, measured with \mathbf{H} perpendicular to the film plane at various temperatures. Open and closed symbols in the MR curve at each temperature correspond to the MR ratios under a left-to-right and right-to-left magnetic field sweeping direction, respectively. Figure 3c shows temperature dependence of MR. Extremely large MR ratios (maximum $\sim 500\%$ at 2 K and 10 kOe) with clear hysteresis were observed. With increasing temperature, the MR ratio decreases remarkably in correlation with the decrease of the resistivity, and shrinks to below 1% at the temperatures above T_C (80 K). Figure 3d shows the MR curves in the four SL samples A1 – A4, measured at 4 K with \mathbf{H} up to 1 T. One can see that the MR ratio increases rapidly from 1 \rightarrow 27 \rightarrow 82 \rightarrow 224% when one goes from sample A1 to A4, in accordance with the decrease of t_{InAs} and the increase of the resistivity.

The strong correlation between the resistivity and the MR ratio clearly implies that spin-dependent scattering of conduction carriers, which are electrons as indicated by Hall measurements, is the dominant scattering mechanism in these FeAs/InAs SL samples. We note that the situation here is very similar to the well-known case of multilayer structures composed of ferromagnetic (FM) / nonmagnetic (NM) metallic layers, in which giant magnetoresistance (GMR) is usually observed. Here, the FeAs layers and InAs spacers play the roles of FM and NM layers, respectively. We thus used a standard two-carrier conduction model usually used for GMR to analyse the large MR observed in our

SL samples. The charge conduction was then divided into up-spin and down-spin channels, with the resistivity of ρ_{\uparrow} and ρ_{\downarrow} , respectively. Using ρ_{\uparrow} and ρ_{\downarrow} , we can rewrite²⁴

$$\text{MR} = \frac{(\rho_{\downarrow} - \rho_{\uparrow})^2}{4\rho_{\downarrow}\rho_{\uparrow}} = \frac{(\alpha - 1)^2}{4\alpha} \quad (3)$$

with $\alpha = \rho_{\downarrow}/\rho_{\uparrow}$ is the spin asymmetry parameter. Due to the spin-dependent scattering at the interfaces of the FeAs layers, α largely deviates from 1. Using equation (3) for the MR of sample A4 (~500% at 2 K), we have an extremely large $\alpha = 22$. There are two possible reasons for this giant value of α : First, it may originate from the large spin-splitting in the conduction band of the FeAs/InAs SLs as revealed by the MCD results (Fig. 2). It is worth noting that for the case of (In,Fe)As we have previously observed the half-metallic conduction band structure⁷. Second, it may originate from high spin-polarization in the DOS of the zinc-blende FeAs layers, because a half-metallic DOS was predicted for bulk FeAs by the first principles calculations¹².

Based on the theoretical framework of GMR²⁴, we quantitatively explain the t_{InAs} -dependence of MR shown in Fig. 3e. In FM / NM multilayers, where GMR appears, the dependence of the MR ratio on the NM layer thickness (t_{InAs}) is given by

$$\text{MR} = \text{MR}_0 \frac{\exp(-\frac{t_{\text{InAs}}}{l_{\text{InAs}}})}{(1 + \frac{t_{\text{InAs}}}{d_0})} . \quad (4)$$

Here MR_0 is the MR magnitude constant, l_{InAs} is the electron mean free path in the InAs spacer, d_0 is an effective length representing the shunting of the current in the FeAs layers. As shown in Fig. 3e, equation (4) provides a very good fitting to the exponential t_{InAs} -dependence of MR with $\text{MR}_0 = 2700\%$, $l_{\text{InAs}} = 1.2$ nm (~4 MLs of InAs) and $d_0 = 0.6$ nm. The short mean free path l_{InAs} of 4 MLs is nearly equal to the thickness of the InAs spacer in sample A4 ($t_{\text{InAs}} = 5$ MLs). This finding is consistent with the fact that the spin-dependent scattering occurs mainly at the FeAs/InAs interfaces. On the other hand, the

value $d_0 = 0.6$ nm is close to the broadening ($\sigma = 0.45$ nm) of the FeAs layers observed by EDX and STEM (Fig. 1). These good agreements strongly suggest that the extremely large MRs in our SL samples can be well understood by the GMR model in semiconductor-based magnetic multilayer systems. These findings also suggest that even higher MR ratios may be obtained in the SLs by optimizing the structure parameter, particularly by using smaller t_{InAs} .

Electrical control of GMR in the FeAs/InAs SL structures

One major advantage of our semiconductor-based magnetic multilayer structures over metallic ones is the ability to control the MR properties using a gate voltage V_G . As shown in Figure 4a, we form an electric double layer field-effect transistor (EDLT) structure using the Hall bar of sample A2 ($N = 3$, $t_{\text{InAs}} = 10$ MLs) (see Methods). As shown in Figs. 4b and c, the resistance and sheet electron concentration n_{2D} in sample A2 are systematically controlled by applying V_G . The change in n_{2D} is small, only 15.5% at $V_G = 5$ V and -7.5% at $V_G = -3$ V. However, as shown in Fig. 4d, significant changes in the MR curves are obtained: The MR ratio at $H = 10$ kOe decreases from 29.2% at $V_G = 0$ V to 22% at $V_G = 5$ V, and increases to 32.3% at $V_G = -3$ V. Again, an increase (decrease) of the MR ratio in accordance with an increase (decrease) of the resistivity is observed. With increasing the electron concentration, the spin-dependent scattering of electron carriers at the FeAs/InAs interface is suppressed due to an enhanced screening effect, which leads to the corresponding decrease in the MR ratio.

DISCUSSIONS

The remaining main question is how the ferromagnetic ground state is induced in the tetrahedral FeAs/InAs SLs of the zinc-blende crystal structure, which contradicts

the prediction by the first principles calculations¹². Indeed, by performing first principles calculations on a FeAs/InAs SL structure with $t_{\text{InAs}} = 5$ ML (see Methods), we deduce a similar conclusion that the magnetic couplings between the substitutional Fe atoms (Fe_δ) in a 1ML FeAs of the SL structure are antiferromagnetic with an exchange energy $J_{ij} = -23$ meV. This result thus suggests that the ground state of the SL system should be antiferromagnetic if *all* the Fe atoms are *ideally* distributed within the 1 ML thickness of the delta-doping zinc-blende FeAs layers (Fe_δ , the red atoms in Fig. 5a and b). However, we surprisingly found that if there is a small amount of disorder where Fe atoms are located in the octahedral interstitial sites (Fe_i , purple atoms in Fig. 5a) and/or in the As sites (Fe_{As} , green atoms in Fig. 5b) which are very close to the 1ML-thick FeAs layer (red plane in Fig. 5a and b), a remarkably stable ferromagnetic ground state can be established. As shown in Fig. 5c and 5d, the magnetic interactions between the Fe_i or Fe_{As} and the Fe_δ (J_{ij}) is ferromagnetic with a very large magnitude of 46 meV, almost double the thermal energy at room temperature. These calculations together with our experimental results can be understood intuitively as follows: All the Fe atoms in our SL structures are in the half-filled Fe^{3+} state, thus the superexchange interaction between the Fe_δ spins prefers antiferromagnetic coupling. However, in the case of pairs of (Fe_i , Fe_δ) or (Fe_{As} , Fe_δ), the atomic distance is much smaller and the direct magnetic coupling, which is ferromagnetic, becomes dominant. As observed in the STEM and EDX mapping (Fig. 1), the broadening of the Fe distribution in the FeAs layer to the nearest upper and lower layers ($\sigma = 1.5$ ML in Fig. 1d) results in the existence of Fe disorders such as Fe_i or Fe_{As} . This disorder-induced ferromagnetic coupling in the FeAs layers is one of the two origins of the overall ferromagnetism in the FeAs/InAs SLs. The other is the interlayer magnetic coupling between the FeAs layers via the RKKY-like interaction, whose manifestation is the

relationship $T_C \sim t_{\text{InAs}}^{-3}$ as mentioned above. We note that the disorder-induced intralayer ferromagnetic coupling does not require itinerant carriers. Meanwhile, the RKKY-like interlayer coupling is rather long-range and requires a sufficient itinerancy of carriers. In resistive samples such as sample A4, although the mean free path of carriers is as short as 1.2 nm (~ 4 ML of InAs) as estimated from the MR results, this mean free path is comparable to the distance t_{InAs} between the FeAs layers (~ 5 ML of InAs in sample A4). Therefore, it is reasonable to conclude that in all the samples (A1 – A4), both the RKKY-like interlayer coupling and disorder-induced intralayer coupling are effective and contribute to establish the overall ferromagnetic order.

The distribution of Fe in the FeAs/InAs superlattices, particularly the presence of Fe disorders, thus plays a key role in determining the magnetic properties of the overall structures. We conduct X-ray absorption fine structure (XAFS) experiments to characterize the local environment of the Fe atoms, together with our first principles calculations. In Fig. 6a, we show the XAFS spectrum measured at the K-edge of Fe (~ 7100 eV) of the sample A4 (7 FeAs layers, with a distance t_{InAs} of 5 monolayers (ML) of InAs). In the inset is the extended X-ray absorption fine structure (EXAFS) oscillation component, whose Fourier transformed spectrum is shown in Fig. 6b (red curve with white circles). There is a large peak at 0.172 nm (pointed by a red arrow), which is much smaller than the distance between the nearest-neighbor atoms (~ 0.262 nm) in a zinc-blende structure of the host InAs (lattice constant $a = 0.606$ nm). These results imply that there are atoms that reside in a closer vicinity, within the distance to the nearest-neighbor atoms, of the substitutional Fe_s atoms in the FeAs layer. We perform a structural optimization using the Vienna *ab initio* simulation package (VASP) code (see Methods) and find that the thickness in the z direction of one FeAs monolayer is 0.165 nm, which

is only 54 % of that in the InAs layer (0.308 nm), in order to accommodate the lattice mismatch (Fig. 6c). In this relaxed structure, the distances d from one Fe_δ atom to the nearest As atom and the two nearest defects, the As-antisite position (Fe_{As}) and the octahedral interstitial defect (Fe_i), are 0.2295 nm, 0.1993 nm, and 0.2325 nm, respectively, as shown in the table in Fig. 6c. Note that Fe_{As} and Fe_i have strong ferromagnetic interactions (~ 46 meV) with the nearest Fe_δ , as explained earlier. Interestingly, the distance d from an Fe_δ atom to the nearest As-antisite Fe_{As} (0.1993 nm) is shorter than the Fe-As distance (0.2295 nm) because the nearest Fe_{As} and Fe_δ atoms attract each other, possibly due to their strong ferromagnetic coupling (see Supplementary Fig. S3). On the other hand, d from a Fe_δ atom to its second-nearest (the In atoms in the next layer) and third-nearest lattice sites (the next Fe_δ atoms) are 0.382 nm and 0.428 nm, respectively, which are too far away and not obvious in the experimental curve shown in Fig. 6b. Therefore, the effects of these second- and third-nearest lattice sites are negligible. Using the calculated results, we simulate EXAFS Fourier-transformed spectra coming from the nearest As atoms in the FeAs layer (black curve), and those from the point defects Fe_{As} (green dotted curve) and Fe_i (purple dotted curve), as shown in Fig. 6b. In the ideal case where all the Fe atoms reside in the substitutional positions Fe_δ of the FeAs layer, the simulated spectrum (black curve) shows a peak at 0.193 nm (pointed by a black arrow), which is still larger than the peak of the experimental spectrum (0.172 nm, pointed by a red arrow). On the other hand, the simulated spectra from Fe_{As} and Fe_i show peaks at 0.160 (pointed by a green arrow) and 0.193 nm, slightly below and above that of the experimental spectrum (0.172 nm). These indicate that only co-existence of different Fe point defects, particularly the antisite Fe_{As} around the Fe_δ atoms, can explain the EXAFS results. By combining the EXAFS data with the first principles calculations, we conclude

that the Fe_{As} and Fe_i point defects are likely responsible for the observed ferromagnetism in the FeAs/InAs .

In conclusion, using the LT-MBE technique, we have successfully grown zinc-blende type FeAs ultrathin layers where the Fe distribution is confined in a thickness of 2 - 3 MLs. By embedding these FeAs quasi-2D layers in an InAs matrix, we have grown FeAs/InAs SL structures, and revealed several unique features that are promising for spintronic applications. In these ferromagnetic SL structures, when decreasing the thickness of the InAs spacer (t_{InAs}), we observed a drastic enhancement of T_C (proportional to t_{InAs}^{-3}), large MR (up to 500% at 2K in the sample with $t_{\text{InAs}} = 5$ MLs), and the very high magnetic moment value of $\sim 5 \mu_B$ per Fe atom. The very large MR ratios were satisfactorily explained by the theory of GMR in FM/NM multilayers, which suggests that the FeAs layers play an important role of FM layers with a very high spin polarization. The MR characteristics can be modulated by applying a gate voltage. Moreover, the strong enhancement of T_C induced by the Fe disorders and RKKY interaction in these FeAs/InAs SLs paves the way for realizing functional magnetic structures for practical spintronic applications at room temperature, which utilises state-of-the-art techniques for controlling the atomic distribution in nanostructures.

METHODS

Calibration of the fluxes of Fe and In

The In flux was calibrated by monitoring the oscillation in RHEED intensity during the MBE growth of InAs on a InAs (001) substrate. The oscillation period corresponds to the time for growing 1 ML of InAs , which enables us to estimate exactly the growth rate of InAs and the flux of In at various temperatures. In the growth of sample A1 – A4, the

growth rate of InAs MLs was fixed to 500 nm/h. The Fe flux was calibrated by measuring the Fe concentration in Fe doped GaAs thin films using secondary ion mass spectroscopy (SIMS) calibrated with Rutherford back scattering (RBS) measurements. In the growth of sample A1 – A4, the growth rate of FeAs layers was fixed to 250 nm/h, corresponding to 4 seconds per 1 ML.

Preparation of the EDLT device

The A3 sample was patterned into a $50 \times 200 \mu\text{m}^2$ Hall bar using standard photolithography and ion milling. A side-gate electrode (G) and several electrodes (including the source S and drain D) for transport measurements were formed via electron-beam evaporation and lift-off of an Au (50 nm)/Cr (5 nm) film. The side-gate pad (G) and the FeAs/InAs SL channel were covered with electrolyte (DEME-TFSI) to form the field-effect transistor (FET) structure. Other regions of the device were separated from the electrolyte by an insulating resist (OMR-100). As illustrated in Fig. 4(a), when a positive V_G is applied, ions in the electrolyte accumulate at the surface of the semiconductor channel and form an electric double-layer capacitor, which works as a nano-scale capacitor. Therefore using V_G we can control the electron concentration in the FeAs/InAs SL structure.

First principles calculations of the FeAs/InAs SLs

We use the KKRnano program developed in Forschungszentrum Jülich on the basis of the all-electron full-potential screened Korringa-Kohn-Rostoker Green's function method^{25,26} based on the density functional theory^{27,28}. The KKRnano program can calculate very large systems with the order-N method in which the numerical effort is scaled linearly with the number of atoms in the supercell²⁹⁻³¹. The Vosko-Wilk-Nussair (VWN) approach to the local density approximation (LDA) was employed for the

exchange-correlation functional^{32,33}. Relativistic effects were included by means of scalar relativistic approximation³⁴. The present calculations were performed with an angular momentum cutoff of $l_{\max} = 2$. For the (In,Fe)As, we performed the calculations on a supercell of 432 atomic positions, being occupied by 90 In, 108 As, 18 Fe atoms in the FeAs layer (Fe_δ), and one additionally doped Fe atom (Fe_i or Fe_{As}), as shown in Fig. 5. This supercell corresponds to the structure of $3 \times 3 \times 3$ zinc blende cell. To discuss quantitatively the magnetic interactions, we calculate the Heisenberg exchange coupling constant (J_{ij}) between the $\text{Fe}_\delta - \text{Fe}_\delta$ atom pairs and that of the $\text{Fe}_\delta - \text{Fe}_i$ atom pairs or $\text{Fe}_\delta - \text{Fe}_{\text{As}}$ atom pairs, on the basis of the Liechtenstein's formula. In the Liechtenstein's formula³⁵, we consider a perturbation by infinitesimal rotations of magnetic moments, according to the magnetic force theorem³⁶. This method has succeeded in quantitatively estimating the magnetic interactions in Fe-based FMS systems.^{37,38}

To examine the local atomic structure, we performed the structural optimization using the Vienna *ab initio* simulation package (VASP)^{39,40,41}, on the basis of the projector augmented wave (PAW) method⁴². We used a supercell containing 128 atomic positions, being occupied by 56 In, 64 As, 8 Fe atoms in the FeAs layer (Fe_δ), and one additionally doped Fe atom (Fe_i or Fe_{As}), as shown in Fig.6c. This supercell corresponds to the structure of $2 \times 2 \times 4$ zinc blende cell. In the supercell calculations, we use $2 \times 2 \times 1$ Monkhorst-Pack⁴³ k -point meshes and set the plane wave cutoff energy to 450 eV. The LDA for exchange-correlation functional was employed.⁴⁴

X-ray absorption fine structure

XAFS measurements were performed at BL5S1 of Aichi Synchrotron Radiation Center with a Si(111) double crystal monochromator. The XAFS spectra were obtained in the partial fluorescence yield mode. The X-ray fluorescence signals were detected by an array

of 7 elements of Si solid state detectors. The monochromator resolution was $E/\Delta E > 7,000$. The EXAFS data were analyzed using the *Athena* and *Artemis* programs. The k^2 -weighted EXAFS oscillations $k^2\chi(k)$ were fitted in the region of $k = 2.9\sim 8.6 \text{ \AA}^{-1}$.

References

1. Kamihara, Y., Watanabe, T., Hirano, M. & Hosono, H. Iron-Based Layered Superconductor $\text{La}[\text{O}_{1-x}\text{F}_x]\text{FeAs}$ ($x = 0.05\text{-}0.12$) with $T_C = 26 \text{ K}$. *J. Am. Chem. Soc.* **130**, 3296–3297 (2008).
2. Hosono, H., Yamamoto, A., Hiramatsu, H., & Ma, Y., Recent advances in Iron-based superconductors towards applications. *Materials Today* **21**, 278-302 (2018).
3. Hai, P. N., *et al.*, Growth and characterization of n-type electron-induced ferromagnetic semiconductor (In,Fe)As. *Appl. Phys. Lett.* **101**, 182403 (2012).
4. Hai, P. N., Anh, L. D., & Tanaka, M., Electron effective mass in n-type electron-induced ferromagnetic semiconductor (In,Fe)As: Evidence of conduction band transport. *Appl. Phys. Lett.* **101**, 252410 (2012).
5. Anh, L. D., Hai, P. N., Kasahara, Y., Iwasa, Y., & Tanaka, M., Modulation of ferromagnetism in (In,Fe)As quantum wells via electrically controlled deformation of the electron wave functions, *Phys. Rev. B* **92**, 161201(R) (2015).
6. Anh, L. D., Hai, P. N., & Tanaka, M., Control of ferromagnetism by manipulating the carrier wavefunction in ferromagnetic semiconductor (In,Fe)As quantum wells. *Appl. Phys. Lett.* **104**, 042404 (2014).
7. Anh, L. D., Hai, P. N., & Tanaka, M., Observation of spontaneous spin-splitting in the band structure of an n-type zinc-blende ferromagnetic semiconductor. *Nature Communications* **7**, 13810 (2016).
8. Anh, L. D., Kaneko, D., Hai, P. N., & Tanaka, M., Growth and characterization of insulating ferromagnetic semiconductor (Al,Fe)Sb. *Appl. Phys. Lett.* **107**, 232405 (2015).
9. Tu, N. T., Hai, P. N., Anh, L. D., & Tanaka, M., Magnetic properties and intrinsic ferromagnetism in (Ga,Fe)Sb ferromagnetic semiconductors. *Phys. Rev. B* **92**, 144403 (2015).
10. Tu, N. T., Hai, P. N., Anh, L. D., & Tanaka, M., High-temperature ferromagnetism in heavily Fe-doped ferromagnetic semiconductor (Ga,Fe)Sb. *Appl. Phys. Lett.* **108**, 192401 (2016).
11. Tu, N. T., Hai, P. N., Anh, L. D., & Tanaka, M., High-temperature ferromagnetism

- in new n-type Fe-doped ferromagnetic semiconductor (In,Fe)Sb. *APEX* **11** (6), 063005 (2018).
12. Griffin, S. M. & Spaldin, N. A., Ab initio investigation of FeAs/GaAs heterostructures for potential spintronic and superconducting applications. *Phys. Rev. B* **85**, 155126 (2012).
 13. Nakamura, T., Anh, L. D., Hashimoto, Y., Iwasaki, Y., Ohya, S., Tanaka, M. & Katsumoto, S., Proximity-Induced Superconductivity in a Ferromagnetic Semiconductor (In,Fe)As. *Journal of Physics: Conference Series* **969** (1), 012036 (2018).
 14. Nakamura, T., Anh, L. D., Hashimoto, Y., Iwasaki, Y., Ohya, S., Tanaka, M. & Katsumoto, S., Evidence for Spin-Triplet Electron Pairing in the Proximity-Induced Superconducting State of an Fe-Doped InAs Semiconductor. *Phys. Rev. Lett.* **122**, 107001 (2019).
 15. Furdyna, J. K., Diluted magnetic semiconductors. *J. Appl. Phys.* **64**, R29 (1988).
 16. Dietl, T., Ohno, H., Matsukura, F., Cibert, J., & Ferrand, D., Zener Model Description of Ferromagnetism in Zinc-Blende Magnetic Semiconductors. *Science* **287**, 1019-1022 (2000).
 17. Vu, N. D., Fukushima, T., Sato, K., & Katayama-Yoshida, H. Materials design of interstitial Be-doped ferromagnetic (In,Fe)As. *Jpn. J. Appl. Phys.* **53**, 110307 (2014).
 18. Chen, X., Na, M., Cheon, M., Wang, S., Luo, H., McCombe, B. D., Liu, X., Sasaki, Y., Wojtowicz, T., Furdyna, J. K., Potashnik, S. J., & Schiffer, P., Above-room-temperature ferromagnetism in GaSb/Mn digital alloys. *Appl. Phys. Lett.* **81**, 511 (2002).
 19. Soo, Y. L., Kioseoglou, G., Kim, S., Chen, X., Luo, H., Kao, Y. H., Sasaki, Y., Liu, X., & Furdyna, J. K., Studies of Mn/GaAs digital alloys using x-ray absorption fine structure and x-ray diffraction methods. *Appl. Phys. Lett.* **80**, 2654 (2002).
 20. Nazmul, A. M., Sugahara, S. & Tanaka, M., Ferromagnetism and high Curie temperature in semiconductor heterostructures with Mn δ -doped GaAs and p-type selective doping. *Phys. Rev. B* **67**, 241308(R) (2003).
 21. Arrott, A., Criterion for Ferromagnetism from Observations of Magnetic Isotherms. *Phys. Rev.* **108**, 1394 (1957).
 22. Bruno, P. & Chappert, C., Oscillatory Coupling between Ferromagnetic Layers Separated by a Nonmagnetic Metal Spacer. *Phys. Rev. Lett.* **67**, 1602 (1991).
 23. Meyer, J., Tombers, M., van Wüllen, C., Niedner-Schatteburg, G., Peredkov, S., Eberhardt, W., Neeb, M., Palutke, S., Martins, M., & Wurth, W., The spin and orbital contributions to the total magnetic moments of free Fe, Co, and Ni clusters. *J.*

- Chem. Phys.* **143**, 104302 (2015).
24. Dieny, B., Giant magnetoresistance in spin-valve multilayers. *J. Magn. Magn. Mater.* **136**, 335 (1994).
 25. Korringa, J., On the calculation of the energy of a Bloch wave in a metal. *Physica* **13**, 392 (1947).
 26. Kohn, W., & Rostoker, N., Solution of the Schrödinger equation in periodic lattices with an application to metallic lithium. *Phys. Rev.* **94**, 1111 (1954).
 27. Hohenberg, P., & Kohn, W., Inhomogeneous Electron Gas. *Phys. Rev.* **136**, B864 (1964).
 28. Kohn, W., & Sham, L. J., Self-Consistent Equations Including Exchange and Correlation Effects. *Phys. Rev.* **140**, A1133 (1965).
 29. Zeller, R., Towards a linear-scaling algorithm for electronic structure calculations with the tight-binding Korringa–Kohn–Rostoker Green function method. *J. Phys.: Condens. Matter* **20**, 294215 (2008).
 30. Thiess, A., Ph.D. thesis, RWTH Aachen (2011).
 31. Thiess, A., Zeller, R., Bolten, M., Dederichs, P. H., & Blügel, S., Massively parallel density functional calculations for thousands of atoms: KKRnano. *Phys. Rev. B* **85**, 235103 (2012).
 32. Vosko, S. H., Wilk, L., & Nusair, M., Accurate spin-dependent electron liquid correlation energies for local spin density calculations: a critical analysis. *Can. J. Phys.* **58**, 1200 (1980).
 33. Vosko, S. H., & Wilk, L., Influence of an improved local-spin-density correlation-energy functional on the cohesive energy of alkali metals. *Phys. Rev. B* **22**, 3812 (1980).
 34. Koelling, D. D., & Harmon, B. N., A technique for relativistic spin-polarised calculations. *J. Phys. C* **10**, 3107 (1977).
 35. Liechtenstein, A. I., Katsnelson, M. I., Antropov, V. P., & Gubanov, V. A., Local spin density functional approach to the theory of exchange interactions in ferromagnetic metals and alloys. *J. Magn. Magn. Mater.* **67**, 65 (1987)
 36. Mackintosh, A. R., & Andersen, O. K., Electrons at the Fermi Surface, *Cambridge University Press, London*, p. 149 (1980).
 37. Shinya, H., Fukushima, T., Masago, A., Sato, K., and Katayama-Yoshida, H., First-principles prediction of the control of magnetic properties in Fe-doped GaSb and InSb. *J. Appl. Phys.* **124**, 103902 (2018).
 38. Fukushima, T., Shinya, H., Masago, A., Sato, K. and Katayama-Yoshida, H., Theoretical prediction of maximum Curie temperatures of Fe-based dilute magnetic

- semiconductors by first-principles calculations. *Appl. Phys. Exp.* **12**, 063006 (2019).
39. Kresse, G., and Hafner, J., *Ab initio* molecular dynamics for liquid metals. *Phys. Rev. B* **47**, 558(R) (1993).
 40. Kresse, G., and Furthmüller, J., Efficient iterative schemes for *ab initio* total-energy calculations using a plane-wave basis set. *Phys. Rev. B* **54**, 11169 (1996).
 41. Kresse, G., and Furthmüller, J., Efficiency of *ab-initio* total energy calculations for metals and semiconductors using a plane-wave basis set. *Comput. Mater. Sci.* **6**, 15 (1996).
 42. Blöchl, P. E., Projector augmented-wave method. *Phys. Rev. B* **50**, 17953 (1994).
 43. Monkhorst, H. J., and Pack, J. D., Special points for Brillouin-zone integrations. *Phys. Rev. B* **13**, 5188 (1976).
 44. Kresse, G., and Joubert, D., From ultrasoft pseudopotentials to the projector augmented-wave method. *Phys. Rev. B* **59**, 1758 (1999).

Acknowledgments

This work was partly supported by Grants-in-Aid for Scientific Research (17H04922, 18H05345, 19H05602, 19K21961, 20H05650), CREST program (JPMJCR1777) and PRESTO Program (JPMJPR19LB) of Japan Science and Technology Agency, and Spintronics Research Network of Japan (Spin-RNJ). Y. I. is supported by the A3 Foresight Program. T. F. acknowledges the support from “Building of Consortia for the Development of Human Resources in Science and Technology” and the Supercomputer Center, the Institute for Solid State Physics, the University of Tokyo.

Authors contribution

Device fabrication, measurements and data analysis: L. D. A, T. H, Y. N; XAFS data analysis: L. D. A, M. K., First principles calculations: H. S, T. F, H. K-Y, writing and project planning: L. D. A, H. K-Y, Y. I and M.T. All authors extensively discussed the results and the manuscript.

Competing financial interests

The authors declare no competing financial interests.

Code availability

The datasets generated during the current study are available from the corresponding author on reasonable request.

Tables and Figures

Table 1| Structure parameters (N , t_{InAs}) and Curie temperature T_C of sample A0 – A4. All samples (except sample A0) have a FeAs/InAs superlattice (SL) structure with a total thickness of 41 – 47 monolayers (MLs), corresponding to 12.4 – 14.2 nm.

Sample	FeAs layer number N	FeAs interlayer distance t_{InAs} (ML)	SL total thickness (nm)	T_C (K)
A0 (ref)	NA	NA	12.0	26
A1	1	20	12.4	5
A2	3	10	13.0	10
A3	5	7	14.2	25
A4	7	5	14.2	80

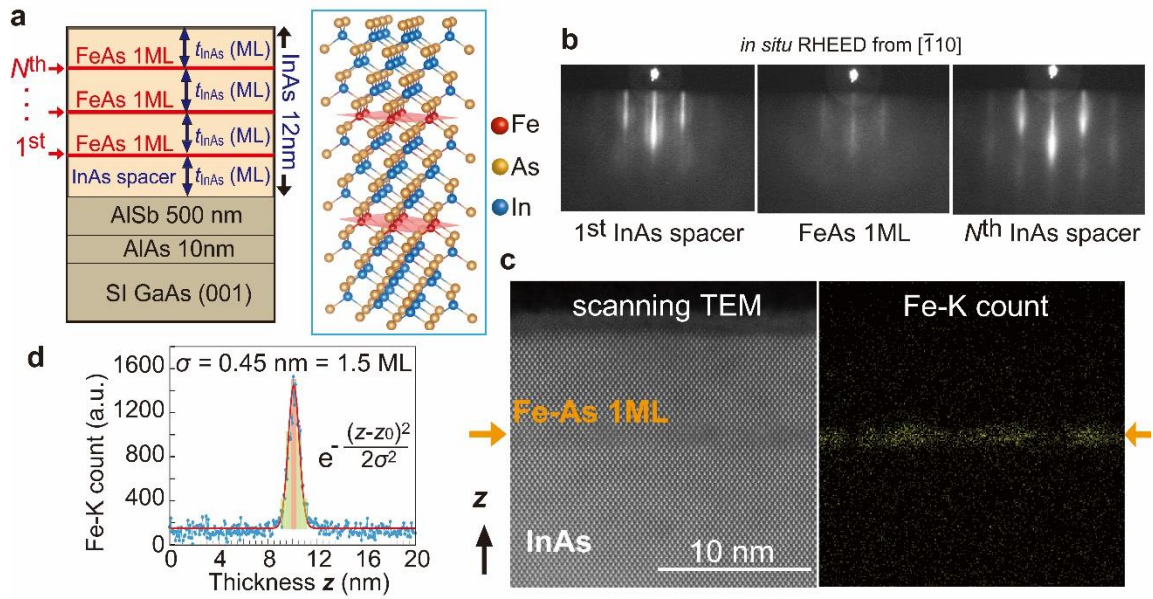


Fig. 1| Crystal growth of FeAs/InAs SL structures. (a) Schematic sample structure of the FeAs/InAs SL grown on a GaAs (001) substrate. There are N FeAs layers embedded in an InAs matrix with a regular distance of t_{InAs} . The total thickness of the FeAs/InAs structures is 41 – 47 MLs (= 12.4 – 14 nm). (b) *In situ* RHEED patterns along the $[\bar{1}10]$ direction during the growth of the FeAs/InAs SL in sample A4. (c) High-resolution scanning TEM of a sample with 1 ML FeAs embedded in InAs (left panel) and the corresponding mapping of Fe atoms by EDX (right panel). (d) Fe distribution along the growth direction mapped with EDX, which follows a normal distribution with a standard deviation of 0.45 nm (1.5 ML of InAs).

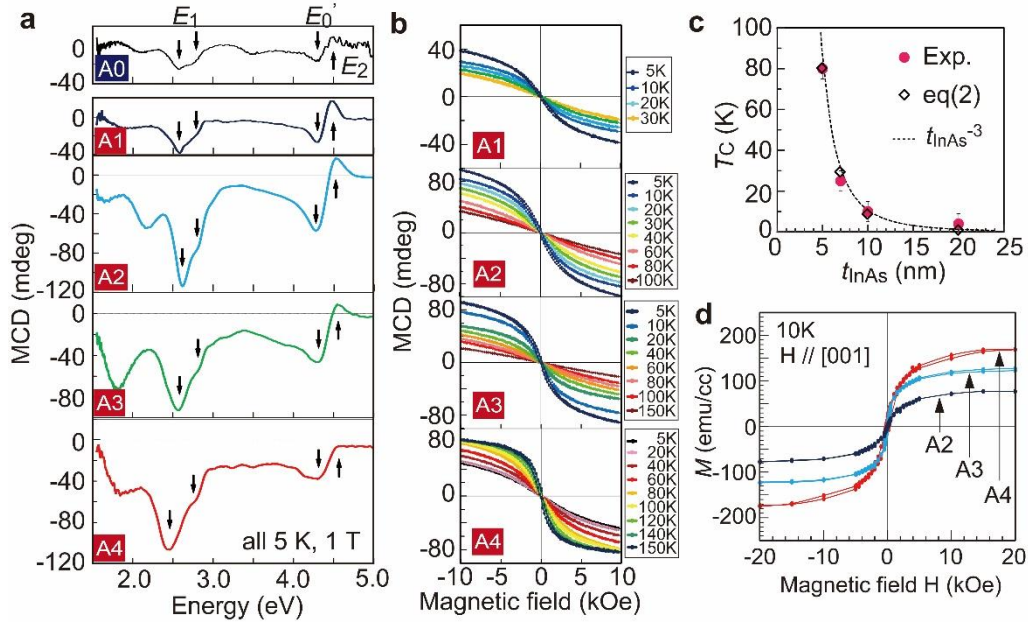


Fig. 2| Magnetic properties of the FeAs/InAs SLs. (a) MCD spectra of sample A1 – A4, compared with that of a reference sample (A0) of 12 nm-thick $(\text{In}_{0.94}\text{Fe}_{0.06})\text{As}$. All spectra were measured at 5 K and 1 T. (b) Magnetic field dependence of MCD intensity (MCD – H curves) measured at E_1 in sample A1 – A4 at various temperatures. (c) Curie temperature (T_C) as a function of the distance t_{InAs} between the FeAs MLs (pink circles). The relationship can be fitted well by the $T_C \sim t_{\text{InAs}}^{-3}$ curve (dotted curve). The T_C values calculated using eq. (2) with $A = 190$ (open diamonds) also well reproduce the experimental results. (d) Magnetic field dependence of magnetization in sample A2 – A4, measured by SQUID magnetometry at 10 K, under a magnetic field perpendicular to the film plane.

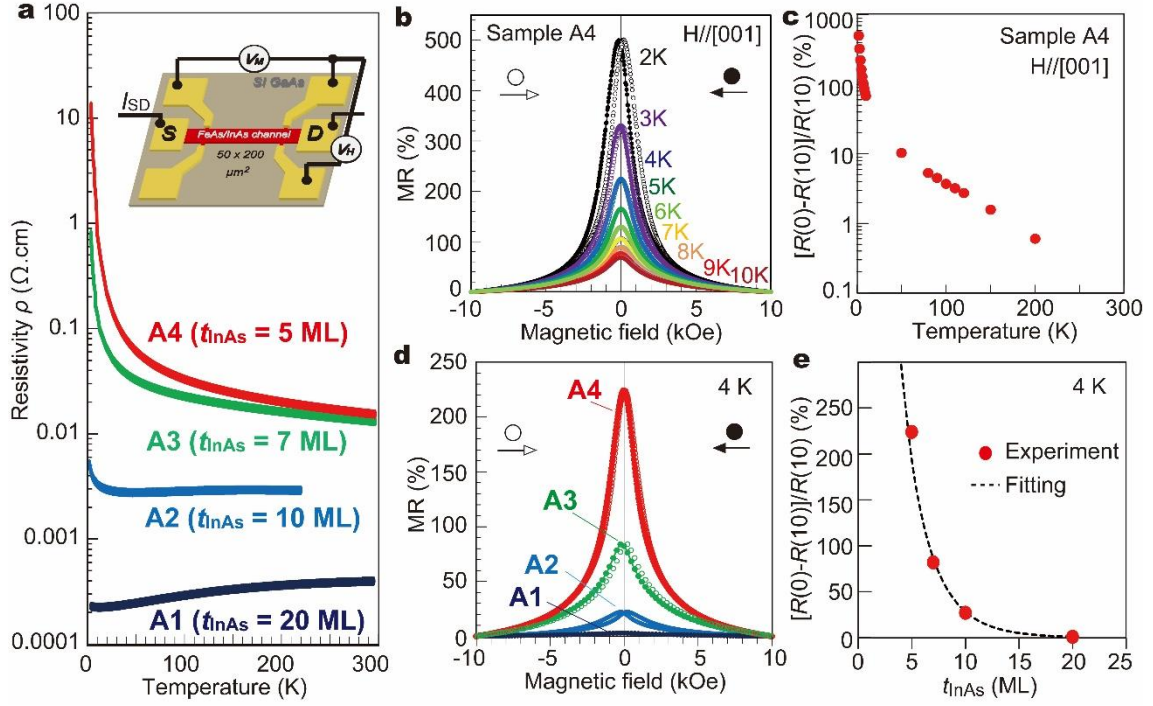


Fig. 3| Magnetotransport properties of the FeAs/InAs SL structures. (a) Temperature dependence of the resistivity in sample A1 – A4. The resistivity was measured by the four terminal method in Hall bars with size of $50 \times 200 \mu\text{m}^2$ (inset). (b) Magnetoresistance (MR) curves measured in sample A4 at various temperatures $T = 2 - 10$ K, when applying a magnetic field perpendicular to the film plane. The MR ratio is defined as $\text{MR}(H) = [R(0) - R(H)]/R(H) \times 100\%$. Open and closed symbols in the MR curve at each temperature correspond to the MR ratios under a left-to-right and right-to-left magnetic field sweeping direction, respectively. (c) MR ratio at $H = 10$ kOe as a function of temperature in sample A4. (d) MR curves measured in sample A1 – A4 at 4 K when applying a magnetic field perpendicular to the film plane. Open and closed symbols correspond to opposite sweeping directions of magnetic field, as described in **b**. (e) MR ratio at $H = 10$ kOe as a function of the distance t_{InAs} between the FeAs layers. The relationship can be fitted well by equation (4) (dotted curve).

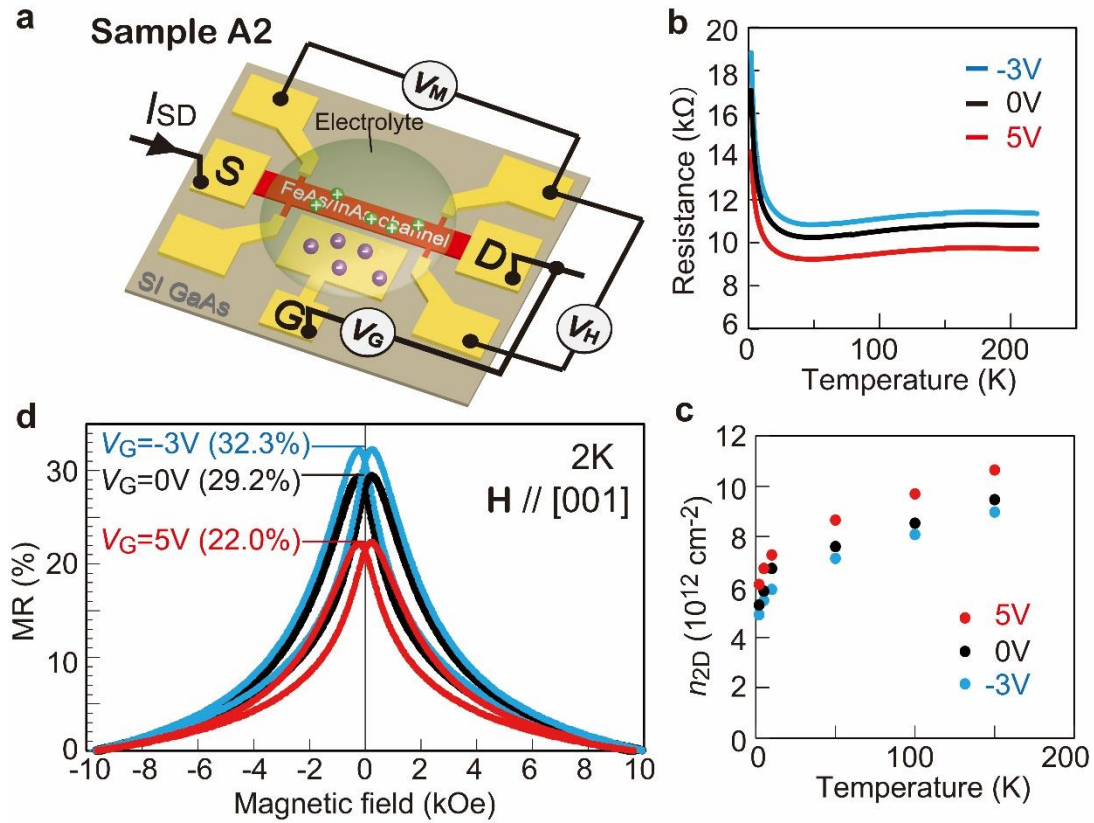


Fig. 4 | Gate voltage control of the magnetoresistance (MR) in FeAs/InAs SLs. (a) Electrical double-layer transistor structure formed on sample A2 (see Method). (b) Resistance and (c) sheet electron density (n_{2D}) in the FeAs/InAs SL structure at various temperatures under different gate voltages $V_G = -3, 0, 5$ V. (d) MR curves measured in the FeAs/InAs SL at 2 K with different gate voltages $V_G = -3, 0, 5$ V, under a magnetic field applied perpendicular to the film plane. These MR curves show clear hysteresis due to the ferromagnetism in sample A2. The values of MR ratio are given in the parentheses after the gate voltages.

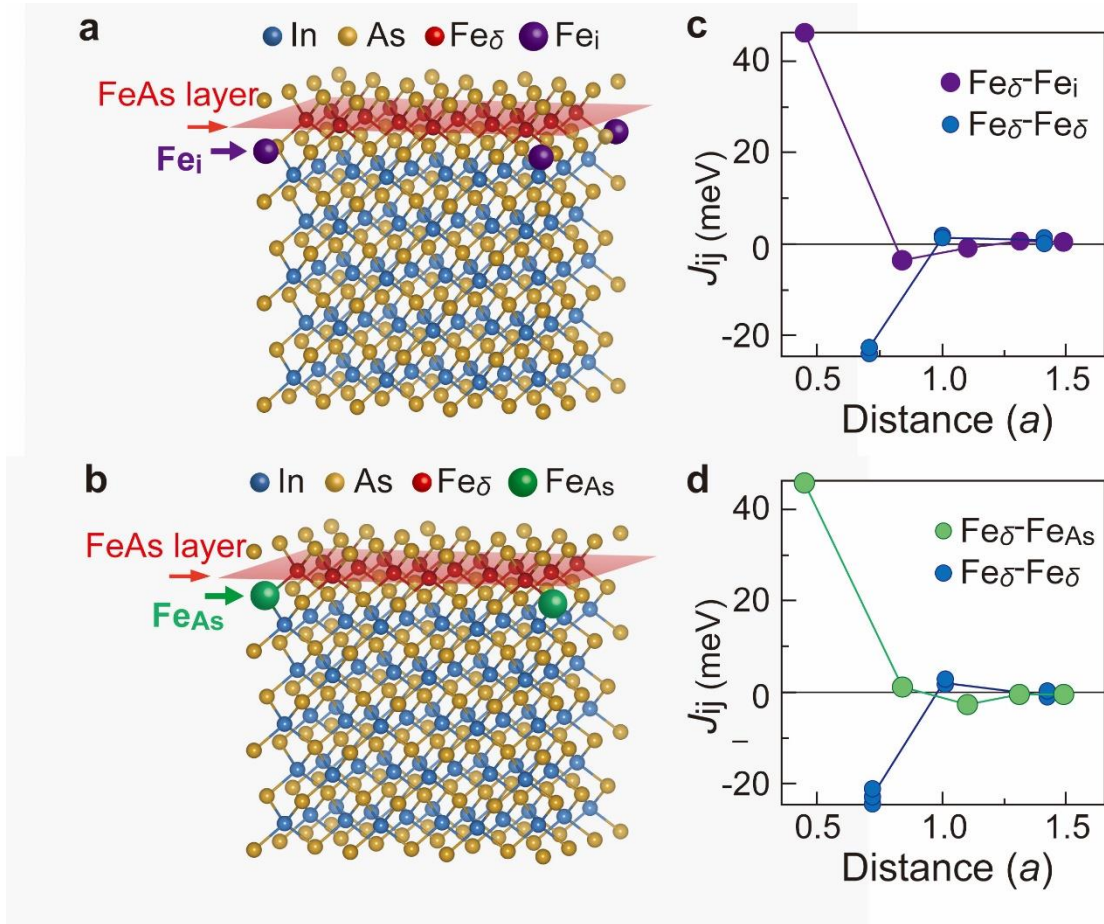


Fig. 5| First principles calculations of Fe-Fe magnetic interactions in FeAs/InAs SLs with Fe disorders. (a),(b) FeAs/InAs SL structure ($t_{\text{InAs}} = 5 \text{ MLs}$) with disordered positions of Fe atoms at the octahedral interstitial site (Fe_i) and As site (Fe_{As}), respectively. (c),(d) Magnetic coupling energy J_{ij} between the Fe spins as a function of distance. Here the distance is expressed with a unit of a ($= 0.302 \text{ nm}$), which is the lattice constant of InAs. Positive (negative) values of J_{ij} represent ferromagnetic (antiferromagnetic) coupling between a pair of Fe spins.

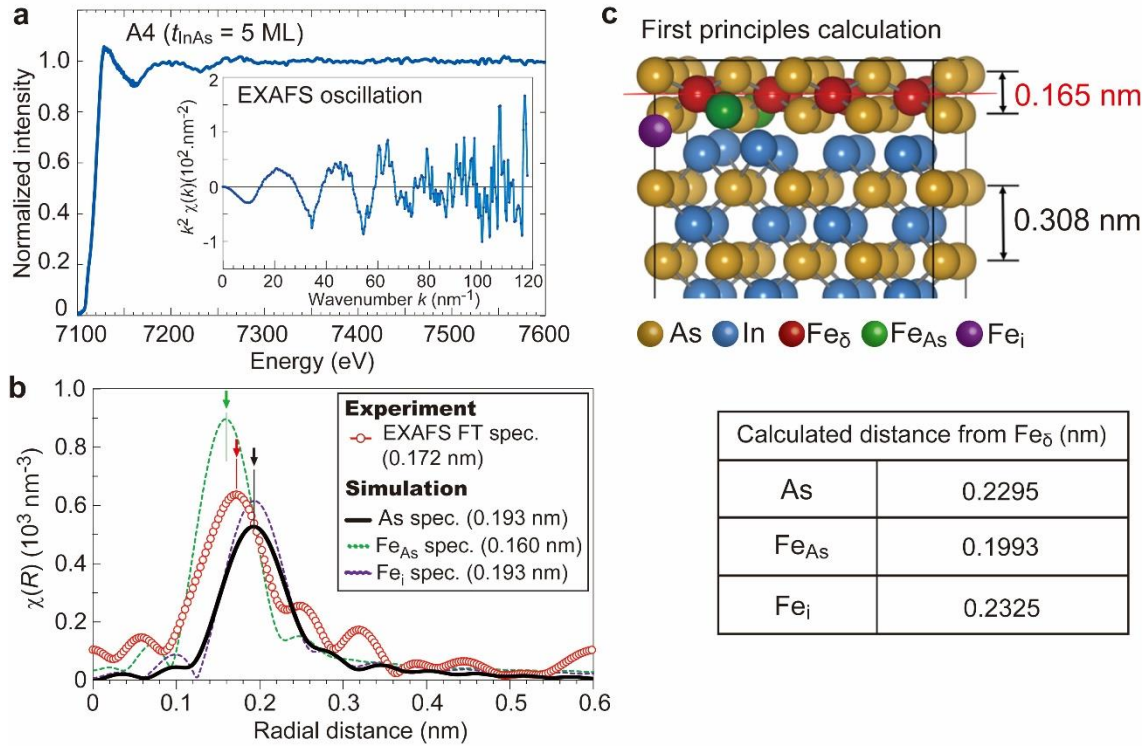


Fig. 6| Local structure around Fe atoms. (a) X-ray absorption fine structure (XAFS) spectrum at the Fe K-edge, measured in sample A4 ($t_{\text{InAs}} = 5$ ML). Inset shows the extended X-ray absorption fine structure (EXAFS) oscillation component extracted from the XAFS spectrum. Here, the EXAFS oscillation is weighted by wavenumber k^2 . (b) The red curve with white circles shows the Fourier transformed (FT) spectrum of the experimental k^2 -weighted EXAFS oscillation shown in (a) as a function of atomic distance. Black curve is the spectrum simulated from the nearest As atoms in the FeAs monolayer, whose lattice in the z direction shrinks as mentioned in (c). Green and purple dotted curves are the spectra simulated from the two Fe disorder positions, As-antisite Fe (Fe_{As}) and octahedral interstitial Fe (Fe_i), respectively, using the atomic distances obtained by our first principles calculation. The peak position of each curve is pointed by an arrow and provided in the legend. (c) First principles calculation shows that the thickness in the z direction of the FeAs layer shrinks to 0.165 nm, which is only 54 % of that (0.308 nm) in the InAs layers. Atomic distances from an Fe atom in the lattice site (Fe_δ) to the nearest As, Fe_{As} , and Fe_i atoms are also shown in the table.

Supplementary Information

Ferromagnetism and giant magnetoresistance in zinc-blende FeAs monolayers embedded in semiconductor structures

Le Duc Anh^{1,2,3*}, Taiki Hayakawa¹, Yuji Nakagawa⁴, Hikari Shinya^{5,6,7}, Tetsuya Fukushima^{7,8,9}, Masaki Kobayashi^{1,9}, Hiroshi Katayama-Yoshida⁹, Yoshihiro Iwasa^{4,10},
and Masaaki Tanaka^{1,9,*}

¹*Dept. of Electrical Engineering and Information Systems, The University of Tokyo, Japan*

²*Institute of Engineering Innovation, The University of Tokyo, Japan*

³*PRESTO, Japan Science and Technology Agency, Japan*

⁴*QPEC & Dept. of Applied Physics, The University of Tokyo, Japan*

⁵*Research Institute of Electrical Communication, Tohoku University, Japan*

⁶*Center for Spintronics Research Network (CSRN), Tohoku University, Japan*

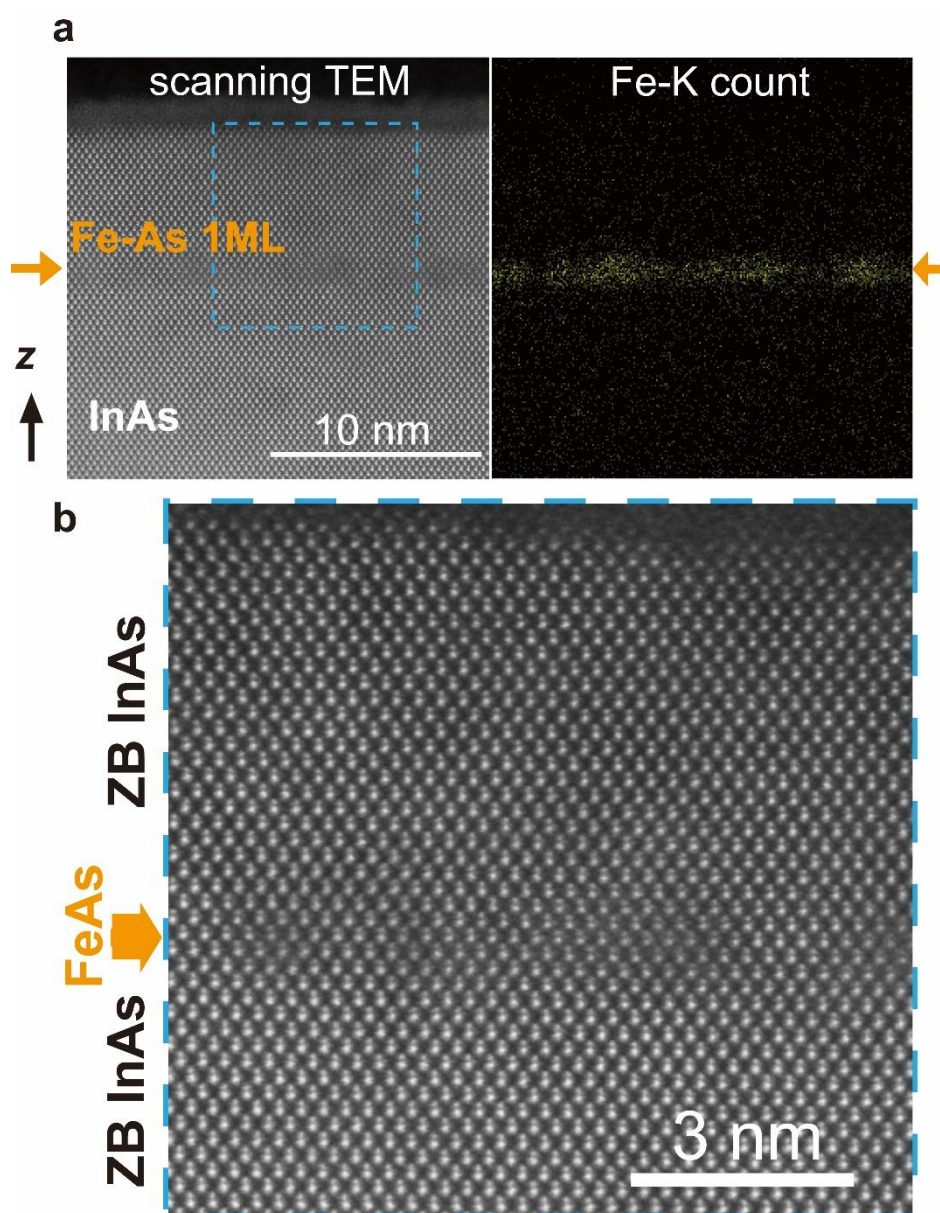
⁷*Center for Spintronics Research Network (CSRN), Osaka University, Japan*

⁸*Institute for Solid State Physics, The University of Tokyo, Japan*

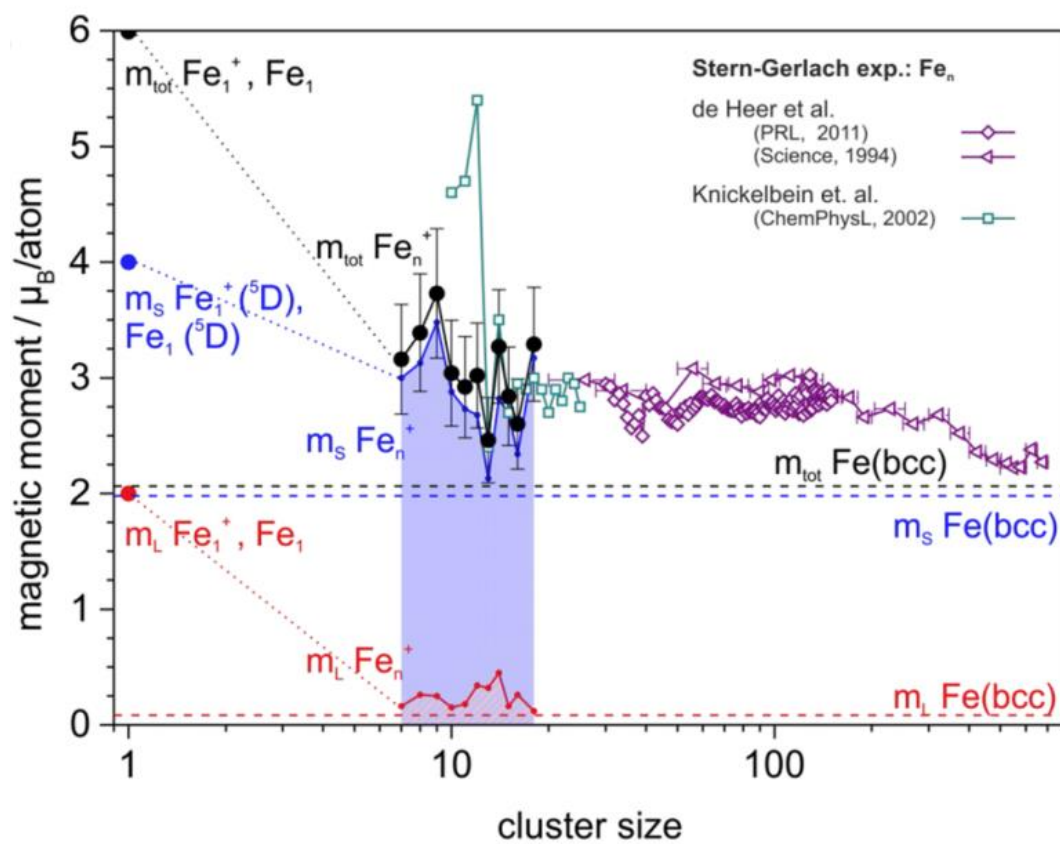
⁹*Center for Spintronics Research Network (CSRN), The University of Tokyo, Japan*

¹⁰*RIKEN Center for Emergent Matter Science (CEMS), Japan*

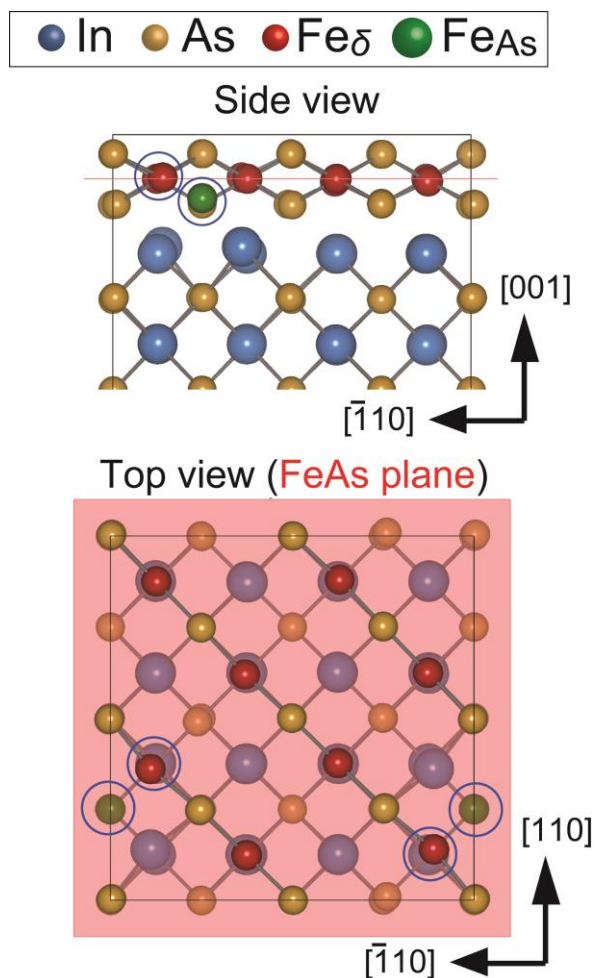
Supplementary Figures and Table



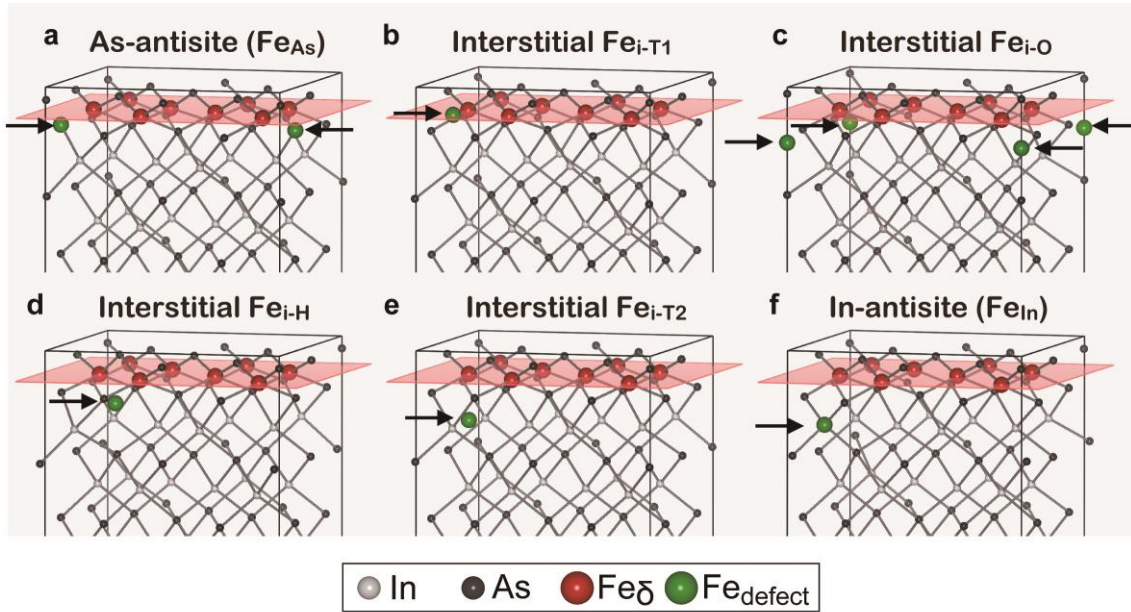
Supplementary Fig S1 | (a) Scanning transmission electron microscopy (STEM) lattice image (left panel) and energy dispersive X-ray spectroscopy (EDX) mapping of Fe atoms (yellow points, right panel) in the sample of one FeAs layer embedded in an InAs matrix. From the EDX mapping, the FeAs layer position can be identified. (b) Magnified STEM lattice image of the FeAs layer embedded in the InAs matrix. The whole area, including the FeAs layer, preserves the zinc-blende crystal structure. It is noteworthy that in the in-plane $[-110]$ direction, the FeAs layer seems to periodically broaden along the growth direction (z axis) with a period of ~ 3 nm. This possibly results from spinodal decomposition of Fe.



Supplementary Fig. S2 | Magnetic moment per atom of Fe cluster depending on the cluster size (number of Fe atoms in the cluster) [adapted from J. Meyer et al., J. Chem. Phys. 143, 104302 (2015)].



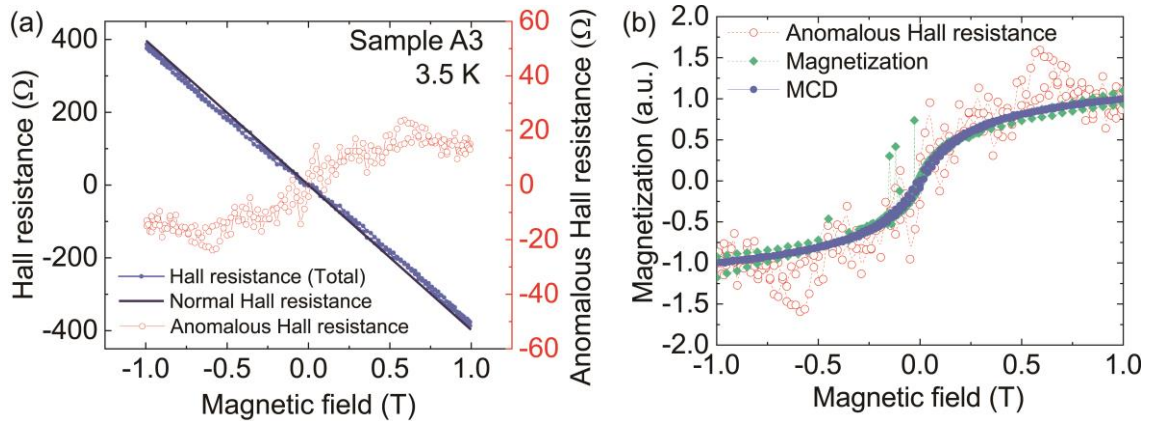
Supplementary Fig. S3| Side view and top views of atomic positions in the case there is one As-antisite Fe (Fe_{As}, green ball) point defect, obtained by our first principles calculations. The nearest Fe_{As} and Fe δ atoms attract each other, possibly due to their strong ferromagnetic coupling, resulting in the smaller atomic distance (0.1993 nm) than the Fe-As bond length (0.2295 nm).



Supplementary Fig. S4 | Several possible Fe-defect positions (green balls, pointed by black arrows) assumed in our first principles calculations, as also summarized in Supplementary Table S1. The substitutional Fe δ atoms in the FeAs layer, In atoms and As atoms are shown by red, gray, and black balls, respectively.

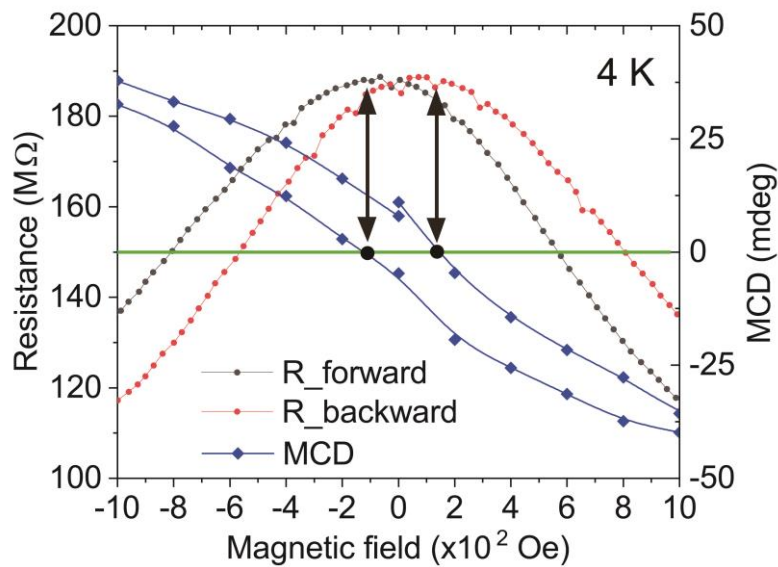
Supplementary Table S1 | Atomic distance from the nearest Fe δ , formation enthalpy, and average magnetic moment per Fe atom of several Fe-defect types, in the order of their distance from the substitutional Fe δ atom in the FeAs layer, calculated by first principles calculations.

Position in Sup. Fig. S4	Fe-defect type	Distance from Fe δ (Å)	Formation enthalpy (eV)	Average magnetic moment/Fe (μ_B)
(a)	As-antisite (Fe _{As})	1.993	2.280	3.375
(b)	Tetragonal interstitial site 1 (Fe _{i-T1} , in the FeAs plane)	2.293	1.101	3.385
(c)	Octahedral interstitial site (Fe _{i-O})	2.325	0.435	3.059
(d)	Hexagonal interstitial site (Fe _{i-H})	2.379	0.443	-
(e)	Tetragonal interstitial site 2 (Fe _{i-T2} , in the next InAs plane)	2.860	-0.311	3.394
(f)	In-antisite (Fe _{In})	3.665	1.893	3.416

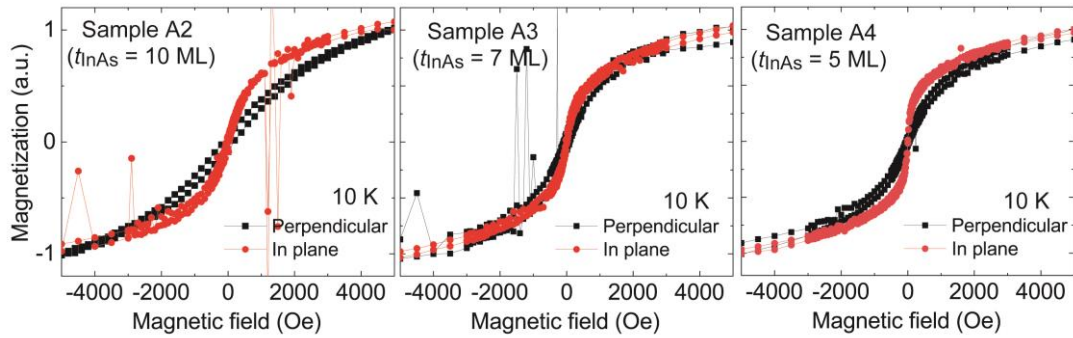


Supplementary Fig S5| Anomalous Hall resistance in the FeAs/InAs superlattices.

(a) Hall resistance (purple circles), which includes a normal Hall resistance (dark blue line) and an anomalous Hall resistance (red open circles, right axis), measured in sample A3 at 3.5 K. (b) Normalized hysteresis loops measured with Hall measurement, MCD, and SQUID in sample A3.



Supplementary Fig S6| Comparison between the coercive forces measured with MCD (blue diamonds) and with magnetoresistance (black and red circles) at 4 K in sample A4. Both measurements show good agreement.



Supplementary Fig S7| Magnetization easy axis in the FeAs/InAs superlattices.

(a),(b),(c) Normalized magnetization curves measured with applying a magnetic field perpendicular to (black squares) and in the plane (red circles) in samples A2, A3, and A4, respectively. All the magnetization curves were measured at 10 K by SQUID, except the curve with a perpendicular magnetic field of sample A2 that was measured by MCD. These data indicate an in-plane magnetization easy axis in these samples.

Supplementary Note 1: Magnetic moment per Fe atom of FeAs/InAs superlattices

The observation of a large magnetic moment close to $5 \mu_B/\text{Fe}$ in our FeAs/InAs superlattices is indeed highly surprising, considering previous values reported in other Fe-As compounds. As can be seen from Supplementary Fig. S2, the magnetic moment of an isolated Fe atom can reach $6 \mu_B/\text{Fe}$, consisting of a spin moment of $4 \mu_B/\text{Fe}$ and an orbital moment of $2 \mu_B/\text{Fe}$. Therefore, if we consider the orbital moment contribution, a value of $5 \mu_B/\text{Fe}$ is possible as an average value of the sum of *the spin moments and orbital moments of Fe atoms* in the lattice sites and defect sites of the FeAs layers, and *the magnetic moments of electron carriers* which are also spin-polarized due to the interactions with Fe spins.

In particular, the orbital moment of a Fe atom in a compound depends strongly on the size and geometry of the compound. For example, in bulk Fe, the orbital moment is frozen out to nearly zero. However, when the cluster size is scaled down, the orbital moment of the Fe atoms at the surface/interface is known to increase due to the lower symmetry [see discussion on the scaling laws of spin and orbital moments in Meyer et al. J. Chem. Phys. 143, 104302 (2015) and the references therein]. In our FeAs/InAs superlattices, the Fe atoms are distributed only in ~ 1 monolayer, neighboring to the InAs layers in both top and bottom interfaces. This *two-dimensional* geometry maximizes the number of Fe atoms at the interfaces, which is likely to induce *a large orbital moment component* in the total magnetic moment. Furthermore, in the first principles calculations we described in the main manuscript and the XAFS measurements (Fig. 6), the most likely positions of Fe in the FeAs/InAs superlattice structures are the lattice sites in the FeAs monolayer (Fe_δ), the As-antisite positions (Fe_{As}), and the octahedral interstitial defects (Fe_i). The interstitial Fe_i atoms form no bonds with surrounding atoms, thus are close to the situation of an isolated Fe. This suggests that the Fe_i atoms might have a high magnetic moment close to $6 \mu_B/\text{Fe}$ and largely contribute to the total magnetic moment. The existence of these Fe defects is different from the other Fe-As compounds usually studied in the context of Fe-based superconductors.

Regarding the magnetic moments of electron carriers, strong magnetic circular dichroism (MCD) signals (~ 100 mdeg, as shown in Fig. 2 in the main manuscript) indicate a largely spin-splitting band structure of the InAs host material. Furthermore, the giant magnetoresistances ($\sim 100\%$, as shown in Fig. 4 of the main manuscript) observed in these structures clearly indicate a strongly unbalanced spin density of states. However, since the electron density in the system is only of the order of $10^{18}\sim 10^{19} \text{ cm}^{-3}$, which is two orders of magnitude smaller than the average Fe density ($10^{20}\sim 10^{21} \text{ cm}^{-3}$), we think

that the magnetic moments contributed from electron carriers are negligible.

According to our first principles calculations using the KKRnano program, which is explained in subsection Methods of the main manuscript, the average magnetic moments per Fe site in the FeAs/InAs superlattices with different types of Fe point defects are about $3.4 \mu_B/\text{Fe}$, as summarized in Supplementary Table S1. These values are still smaller than that observed experimentally ($4.7 - 4.9 \mu_B/\text{Fe}$). In first-principles calculations, it has been well known that the local density approximation (LDA) often fails to describe the localized d states in transition metal elements, leading to underestimation of the exchange splitting energies and local magnetic moments. The LDA with the self-interaction correction (SIC-LDA) method improves these shortcomings and gives reasonable results consistent with the experiments, such as in the cases of (Ga,Mn)N, (Ga,Mn)As, (Zn,TM)O, and (Ge,Fe) [*Phys. Status Solidi* **3**, 4155 (2006), *Physica B* **376**, 647 (2006), *Phys. Rev. B* **96**, 104415 (2017)]. In our large-scale all-electron calculations, however, it is quite difficult to apply the SIC-LDA method; therefore, we are employing LDA for the exchange correlation functional. Moreover, we do not consider the spin-orbit interaction in the calculations, thus the contribution of the orbital magnetic moments to the total moment is ignored. In the present case, since the system behaves as n-type, the electrons which occupy the minority spin states generate finite orbital magnetic moments. The LDA error and the ignoring the spin orbit interaction (i.e., orbital moment) are thought to be the cause of the deviation between the experimental and calculated Fe magnetic moments.

Supplementary Note 2: Calculated formation enthalpy values of many Fe defects in the FeAs/InAs superlattices

We calculated the formation enthalpy values of many Fe defects, shown in Supplementary Fig. S4, using the Vienna *ab initio* simulation package (VASP) code, whose details are given in the Methods. The formation enthalpy of the octahedral interstitial Fe_i is the second lowest, after the tetragonal interstitial Fe in the next InAs layer (see Supplementary Table S1). However, we would like to note that first-principles calculations are basically valid only in the thermal equilibrium state. In the present experiments, the FeAs/InAs superlattices were grown at very low temperature ($\sim 220^\circ\text{C}$) which is a non-equilibrium MBE growth process. Thus, the situation may be considerably different from that at the thermal equilibrium state. Therefore, the antisite Fe_{As} defects may still be formed although the calculated formation enthalpy is high. We note that at this low growth temperature ($\sim 220^\circ\text{C}$), the Fe:As and In:As flux ratios are kept very close to 1:1, which are much lower than those ($\sim 1:10$ to $1:20$) at an equilibrium growth process

of InAs at much higher temperature (450 – 500°C). This low As flux may induce the formation of As-antisite defects in our samples.

Supplementary Note 3: Anomalous Hall effect in the FeAs/InAs superlattices

We observed the anomalous Hall effect in our samples. Supplementary Figure S5a shows Hall resistance data measured in sample A3 (5 layers of FeAs) at 3.5 K. The observation is quite challenging because the anomalous Hall resistances (AHR) in these samples are small. As can be seen in Supplementary Figure S5a, the AHR component is only 5% of the total Hall resistance and is almost hidden by the normal Hall resistance component. This feature is similar to that of n-type FMS (In,Fe)As [see LDA et al., Phys. Rev. B **92**, 161201(R) (2015)]. This small AHR is expected in n-type ferromagnetic semiconductors because of the weak spin-orbit interaction in the conduction band (weaker than that in the valence band). Furthermore, the samples with strong ferromagnetism such as A2, A3 and A4 are highly resistive, which further hinders the Hall measurements. As a result, the AHR component is noisy as can be seen in Supplementary Fig. S5. Nevertheless, the magnetic hysteresis loops obtained from AHR, MCD, and SQUID measurements agree very well with others, as shown in Supplementary Fig. S5b. Moreover, as shown in Supplementary Fig. S6, the hysteresis loops measured with magnetoresistance (MR) and with MCD in sample A4 agree with each other very well (The coercive forces are ± 188 Oe). These data indicate that the ferromagnetism in the FeAs/InAs samples is intrinsic and single-phase.

Supplementary Note 4: Magnetic circular dichroism (MCD) intensity in the FeAs/InAs superlattices of samples A2, A3, A4

The magnetization per layer in all the samples are virtually same, similar values of $2.42 - 2.49 \times 10^{-5}$ emu/cm². Therefore, the magnetization in these samples should scale up with the number of FeAs layers. Consequently, the MCD intensity, which is proportional to the magnetization, should also increase from sample A1 to A4. Indeed, the MCD intensity of sample A2 is double that of sample A1. However, it stays constant (~100 mdeg) in sample A2, A3 and A4 (see Fig. 2 in the main manuscript). We think that this is due to a short penetration depth of the incoming light in these FeAs/InAs superlattice structures: The MCD effectively measures into a depth corresponding to only three FeAs/InAs periods. This is a possible scenario, because the narrow-gap InAs host strongly absorbs visible light (200 – 800 nm). Moreover, the superlattice structure and the mid-gap states introduced by FeAs layers may enhance the light absorption and further

limit the penetration depth.